Geochemistry
Geophysics
Geosystems
$G^3$

Published by AGU and the Geochemical Society

*Article*
Volume 14, Number 10
21 October 2013
doi: 10.1002/ggge.20275
ISSN: 1525-2027

# Distinctive upper mantle anisotropy beneath the High Lava Plains and Eastern Snake River Plain, Pacific Northwest, USA

**Lara S. Wagner**
*Department of Geological Sciences, University of North Carolina, Chapel Hill, North Carolina, 27599, USA (wagner@unc.edu)*

**Maureen D. Long**
*Department of Geology and Geophysics, Yale University, New Haven, Connecticut, USA*

[1] The Pacific Northwest (PNW) has experienced voluminous intraplate volcanism over the past ~17 Ma, beginning with the Steens/Columbia River flood basalts and continuing with the still-ongoing volcanism in the High Lava Plains (HLP) and eastern Snake River Plain (SRP). Here we present two complementary datasets (SKS splitting and Rayleigh wave phase velocity anisotropy) that place constraints on the anisotropic structure of the upper mantle beneath the HLP and SRP regions. Beneath the HLP, SKS phases reveal dominantly E-W fast splitting directions and large (up to ~2.7 s) delay times, with pronounced lateral variations in $\delta t$. Lateral and depth variability in the strength of anisotropy beneath the HLP is also evident from Rayleigh wave dispersion. Beneath the SRP, SKS splitting delay times are much smaller (~0.5 s), and surface wave observations suggest a region of upper mantle anisotropy (~50–150 km depth) with a geometry that deviates significantly from the generally plate motion parallel fast directions observed just outside of the SRP. Beneath the HLP, the geometry of the anomalously strong anisotropy is similar to the anisotropy in the deeper parts of the upper mantle, resulting in constructive interference and large SKS splitting delay times. Beneath the SRP, the geometry of the anomalous anisotropic region in the shallow mantle is different, resulting in destructive interference and reduced SKS splitting delay times. We discuss several possible explanations for these observations, including variations in olivine lattice-preferred orientation (LPO) strength, transitions in olivine fabric type, and a contribution from aligned partial melt.

**Components:** 12,914 words, 9 figures.

**Keywords:** anisotropy; Rayleigh waves; shear wave splitting; high lava plains; Snake River Plain; Yellowstone.

**Index Terms:** 8137 Hotspots, large igneous provinces, and flood basalt volcanism: Tectonophysics; 8110 Continental tectonics: general: Tectonophysics; 8178 Tectonics and magmatism: Tectonophysics; 8180 Tomography: Tectonophysics; 7270 Tomography: Seismology.

**Received** 4 June 2013; **Revised** 4 September 2013; **Accepted** 18 September 2013; **Published** 21 October 2013.

Wagner, L. S., and M. D. Long (2013), Distinctive upper mantle anisotropy beneath the High Lava Plains and Eastern Snake River Plain, Pacific Northwest, USA, *Geochem. Geophys. Geosyst.*, *14*, 4647–4666, doi:10.1002/ggge.20275.

## 1. Introduction

[2] The western United States has a rich and complicated recent tectonic history [e.g., *Humphreys and Coblentz*, 2007], which over the past ~20 Ma has encompassed the rollback and steepening of the Farallon slab, the northward migration of the Mendocino Triple Junction, extension in the Basin and Range, the outpourings of the Steens/Columbia River flood basalts (S/CRB), and likely episodes of localized lithospheric delamination [*Zandt et al*., 2004; *West et al*., 2009]. Even in this complex tectonic setting, the High Lava Plains (HLP) of Oregon and the eastern Snake River Plain (SRP) of Idaho stand out as distinctive features. The HLP represents a bimodal volcanic province that over the past ~12 Ma has exhibited both age-progressive rhyolitic volcanism [*Jordan et al*., 2004, *Ford et al*., 2013] and widespread basaltic volcanism [*Till et al*., 2013] with no obvious spatiotemporal pattern. The age-progressive trend in the HLP rhyolites is oblique to the absolute plate motion of the North American plate, in contrast to the Yellowstone/Snake River Plain (Y/SRP) trend to the east. The spatiotemporal trend in rhyolitic volcanism beneath the SRP is roughly parallel to the absolute motion of the North American plate [*Pierce and Morgan*, 1992] and also corresponds to the preexisting lithospheric structure of the western Idaho shear zone [*Tikoff et al*., 2008]. Many different models have been proposed to explain the origin and evolution of the S/CRB, HLP, and SRP volcanic trends [e.g., *Hooper et al*., 2007]. These models variously invoke a deep mantle plume [*Armstrong et al*., 1975; *Richards et al*., 1989; *Camp and Ross*, 2004; *Smith et al*., 2009; *Obrebski et al*., 2010; *Kincaid et al*., 2013], the rollback, steepening, tearing, and/or fragmentation of the Juan de Fuca slab at depth [*Carlson and Hart*, 1987; *James et al*., 2011; *Liu and Stegman*, 2012; *Long et al*., 2012], lithospheric delamination [*Hales et al*., 2005; *Camp and Hanan*, 2008; *Darold and Humphreys*, 2013], and/or preexisiting lithospheric structures [e*Cross and Pilger*, 1978; *Tikoff et al*., 2008] as playing a role in generating volcanism.

[3] The recent interdisciplinary High Lava Plains Project (www.dtm.ciw.edu/research/HLP), along with the EarthScope USArray Transportable Array (TA), has provided a wealth of new geophysical data in the region. In particular, recent studies using body wave [*Roth et al*., 2008; *Schmandt and Humphreys*, 2010; *James et al*., 2011; *Obrebski et al*., 2011], surface wave [*Warren et al*., 2008; *Wagner et al*., 2010, 2012a], and ambient noise [*Gao et al*., 2011; *Hanson-Hedgcock et al*., 2012] tomography, receiver function analysis [*Eagar et al*., 2010, 2011; *Schmandt et al*., 2012], and SKS splitting measurements [*Long et al*., 2009] have yielded new insight into the structure of the crust and upper mantle beneath the HLP and SRP. One of the most striking geophysical characteristics of the HLP is the strong seismic anisotropy in the upper mantle beneath it. SKS splitting measurements for the western United States [*Zandt and Humphreys*, 2008; *Liu*, 2009; *Eakin et al*., 2010; *Long et al*., 2012] reveal strong splitting with large (>2 s) delay times beneath the HLP, and models that incorporate surface wave data also generally show strong upper mantle anisotropy in this region [e.g., *Yuan and Romanowicz*, 2010; *Lin et al*., 2011; *Lin and Ritzwoller*, 2011]. A study of SKS splitting beneath eastern Oregon that incorporated data from the first phase of the HLP experiment showed that stations in southeastern Oregon exhibit average delay times up to ~2.7 s [*Long et al*., 2009], much larger than the ~1 s that is typical for continental regions [*Silver*, 1996].

[4] One of the most striking geophysical characteristics of the SRP is the zone of very low upper mantle velocities that is ubiquitous beneath the SRP volcanic track. This low-velocity region takes the form of a roughly linear (in map view) feature that extends to depths of ~150–200 km [e.g., *Stachnik et al*., 2008; *Schmandt and Humphreys*, 2010; *James et al*., 2011; *Obrebski et al*., 2011], deepening slightly beneath Yellowstone [*Wagner et al*., 2010]. The origin of this uppermost mantle structure continues to be debated, but recent electromagnetic imaging has suggested that the zone of particularly low wavespeeds coincides with relatively high conductivities [*Kelbert et al*., 2012], consistent with the presence of partial melt. Interestingly, unlike the HLP, the SRP has not been associated with particularly strong upper mantle anisotropy in past studies. Specifically, *Schutt et al*. [1998] measured SKS splitting for a linear transect deployed perpendicular to the strike of the SRP and found a pronounced decrease in splitting delay times above the SRP proper. Later work by *Waite et al*. [2005], which focused on a region to the east of the *Schutt et al*. [1998] transect, did not identify a decrease in $\delta t$ values beneath the SRP and instead found delay times of ~ 1 s, comparable to the surrounding region.

[5] Seismic anisotropy is an important observable for understanding mantle processes because of the link between mantle deformation and the resulting

anisotropy [e.g., *Long and Becker*, 2010]. In the upper mantle, seismic anisotropy is usually attributed to the lattice-preferred orientation (LPO) of anisotropic minerals, primarily olivine [e.g., *Karato et al*., 2008]. If the geometrical relationship between strain and the resulting anisotropy is known or assumed, then measurements of seismic anisotropy can be used to infer the pattern of mantle flow and deformation, giving seismologists one of the most powerful tools available to probe mantle dynamics with seismologic observations. While the geometry of mantle anisotropy is very often used to infer mantle flow patterns, the strength of anisotropy is more difficult to constrain observationally and thus more difficult to exploit to gain insight into mantle deformation. In particular, the poor depth resolution of SKS phases means that estimates of anisotropy strength from splitting measurements trade off directly with estimates of the thickness of the anisotropic layer. While surface wave measurements can provide depth constraints, it is a challenge to properly constrain the magnitudes of anisotropic anomalies in a regularized tomographic inversion of surface wave dispersion data. Although it is difficult to constrain, the strength of anisotropy is potentially important as it is related to upper mantle conditions during deformation, such as the amount of strain, olivine fabric type, mineralogy, and/or partial melt fraction [*Karato et al*., 2008].

[6] Here we take advantage of the data sets provided by the HLP broadband seismic experiment and the USArray Transportable Array (TA) and apply SKS splitting analysis and surface wave inversion to understand the lateral and depth variations in the strength of anisotropy beneath the Pacific Northwest, with a particular focus on the HLP and SRP. The very dense station spacing of the HLP deployment [*Carlson et al*., 2005] allows us to use SKS splitting to obtain robust constraints on small-scale lateral variations in splitting delay times, $\delta t$, beneath the HLP proper. In combination with surface wave inversions that yield information about the depth extent of the anisotropy, we are able to obtain a robust picture of lateral and depth variations in upper mantle anisotropy beneath the PNW region. Beneath the HLP, we find evidence for pronounced lateral gradients in anisotropic strength, with a region of particularly strong uppermost mantle anisotropy that coincides spatially with Holocene basalt volcanism. Given the relatively simple flow field beneath the region inferred from previous studies of anisotropy [*Long et al*., 2012], these variations may indicate lateral variations in the strength and/or geometry of olivine fabric, or in the amount or alignment of partial melt. Beneath the SRP, we find evidence for a layer of weak to moderate anisotropy with a strikingly different geometry than the surrounding regions of the upper mantle overlying a more strongly anisotropic layer more closely oriented to APM. This region coincides spatially with the region of extremely low wavespeeds inferred from seismic tomography [e.g., *Wagner et al*., 2010, 2012a; *James et al*., 2011] and high conductivity inferred from magnetotelluric (MT) measurements [*Kelbert et al*., 2012]. We discuss several plausible scenarios to explain the distinctive anisotropy we infer beneath both the HLP and SRP.

## 2. Data and Methods

### 2.1. SKS Splitting

[7] The SKS splitting data set presented here represents an update to the work of *Long et al*. [2009], who analyzed data from TA stations in eastern Oregon and the surrounding region as well as data from the first year of the HLP seismic deployment (through October 2008). Here we present the final version of the HLP experiment SKS splitting data set, which also includes data recorded at HLP stations for the period October 2008–September 2009 (Figure 1). This yields an additional ~20 stations that were not included in our original analysis, and the addition of the extra year of HLP data also allows us to estimate more robustly the average SKS delay times at each station. We followed the data preprocessing and measurement procedures of *Long et al*. [2009]; briefly, we selected SKS phases for events in the 88°–130° epicentral distance range for processing. A bandpass filter with corner frequencies of 0.1 and 0.01 was applied; in a minority of cases, we adjusted the filter parameters manually to optimize waveform clarity for individual arrivals. We used the SplitLab software [*Wüstefeld et al*., 2008] to estimate splitting parameters using the rotation-correlation and transverse component minimization methods simultaneously. All measurements were assigned a quality measurement of "good" or "fair," according to the classification used by *Long et al*. [2009].

[8] A striking aspect of the HLP SKS splitting data set is the strong splitting with relatively uniform fast directions and little variation with event backazimuth that we observe at HLP stations, suggesting a relatively simple anisotropic geometry. Backazimuthal coverage for SKS phases in the

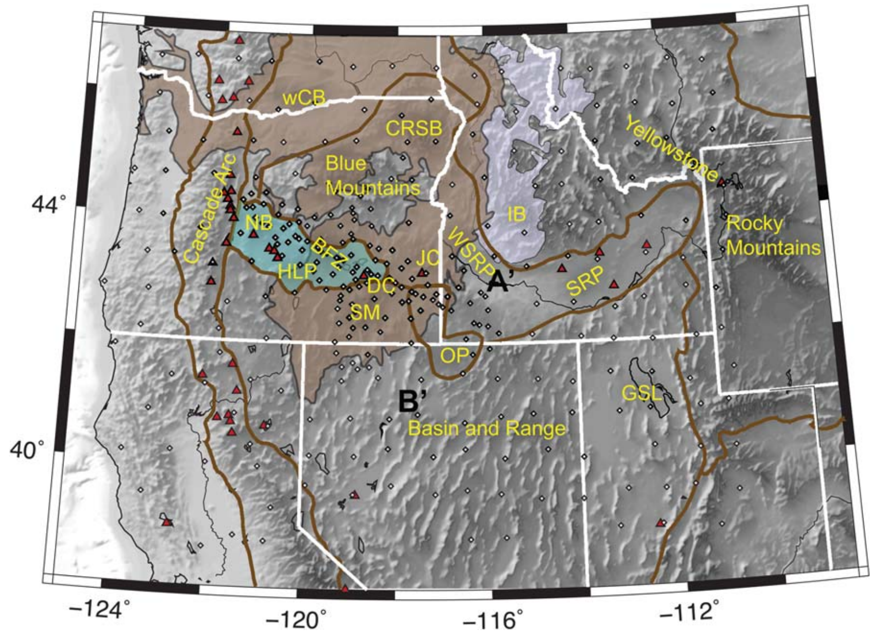

**Figure 1.** Tectonic map of the Pacific Northwest: Brown shaded region indicates the area covered by the Columbia River and Steens flood basalts (CRSB). Red triangles indicate Holocene volcanoes. Solid white lines are state boundaries. Brown lines indicate boundaries for physiographic provinces from the USGS (http://tapestry.usgs.gov/physiogr/physio.html), modified to include the boundary of the High Lava Plains (light blue shaded area) from *Meigs et al*. [2009] and the Owyhee Plateau from *Shoemaker* [2004]. Other features noted: Idaho Batholith (IB; light shaded area); Snake River Plain (SRP); Western Snake River Plain (WSRP); western Columbia Basin (wCB); Owyhee Plateau (OP); Great Salt Lake (GSL); Newberry Volcano (NB); High Lava Plains (HLP), Diamond Craters (DC), Jordan Craters (JC).

western United States is heavily weighted toward the western Pacific subduction zones, precluding a complete investigation of the backazimuthal variability, but for many stations, we were able to achieve some coverage of two to three backazimuthal quadrants. In general, we do not observe meaningful variations in measured splitting parameters with backazimuth beneath the HLP, and the null SKS arrivals we observe at HLP stations arrive from backazimuths that are consistent with the observed fast directions for split SKS arrivals. This is demonstrated by a representative sampling of single-station SKS splitting patterns for stations located within the HLP, as shown in Figure 2. Here we show examples of typical splitting patterns as a function of event backazimuth for six TA and HLP experiment stations; for each of the patterns shown, the fast directions do not vary significantly with backazimuth, and the non-split SKS arrivals generally come from backazimuths that are consistent with the observed $\phi$. This simplicity in the observed splitting patterns suggests that in general, anisotropy beneath the HLP can be described with a single anisotropic layer with a roughly horizontal axis of symmetry, as we do not observe the complications that would be expected for multiple anisotropic layers [*Silver and Savage*, 1994]. This is in contrast to some of the regions surrounding the HLP, such as the Blue and Wallowa Mountains, which do exhibit significant variability in splitting parameters with backazimuth. This variability has been interpreted as being due to multiple layers of anisotropy, likely corresponding to distinctive anisotropic geometries in the mantle lithosphere and the underlying asthenosphere [*Long et al*., 2009].

[9] Given this apparent simplicity, it is appropriate to represent SKS splitting beneath eastern Oregon by taking single-station averages of the highest-quality measured splitting parameters ($\phi$, $\delta t$) at each station, as shown in Figure 3 and in supporting information,[1] Table S1. Our single-station averages were obtained by taking nonweighted, simple averages of measured delay times and circular averages of fast directions for the set of highest quality measurements at each station. For the vast majority of stations, this corresponds to all "good" quality measurements; for a few stations,

---

[1] Additional supporting information may be found in the online version of this article.

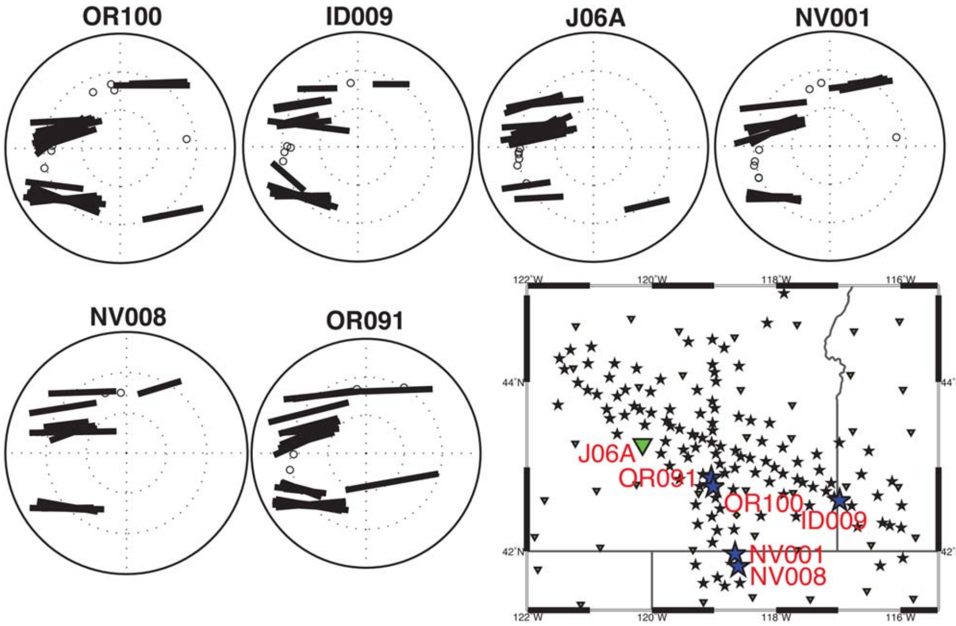

**Figure 2.** Stereoplots of representative splitting patterns (measured splitting parameters as a function of event backazimuth) for six stations located in the HLP region. Both "good" and "fair" quality measurements are shown, plotted as sticks oriented in the fast direction and whose lengths are proportional to the delay times. Null measurements are plotted with a circle at the event backazimuth. Map shows location of HLP (stars) and TA (triangles) stations; locations of six selected stations are shown with large symbols and are labeled with station name.

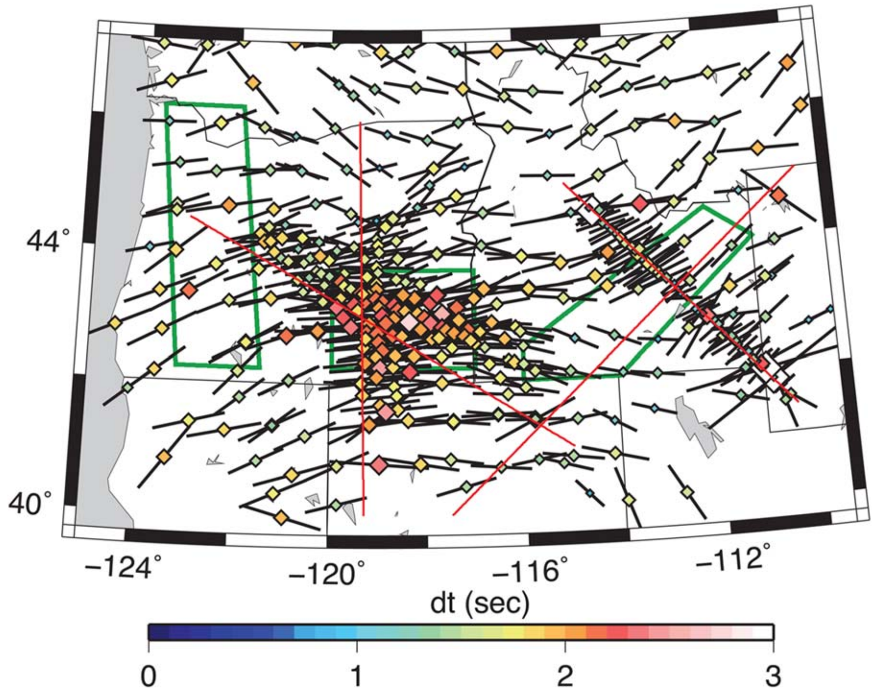

**Figure 3.** SKS single-station average splitting map. Colors of diamonds and length of black bars indicate splitting delay time (sec). Bars indicate anisotropic fast directions. Data from this study are obtained from *Schutt et al*. [1998] and *Fouch and West* [2008]. Red lines locate cross sections shown in Figures 5–9. Green boxes indicate the bounds of the anisotropic areas described in section 2.3.1 and Figure 5.

this corresponds to all "fair" quality measurements. The backazimuthal distribution of null (i.e., nonsplit) SKS arrivals were not taken into account in our averaging scheme; given the simplicity of the splitting patterns documented in Figure 2, this is appropriate. We also experimented with other averaging schemes, including using all "good" and "fair" measurements for each station, but found that the type of averaging scheme made very little difference in the overall estimates.

## 2.2. Rayleigh Wave Phase Velocity Inversions

[10] The data and methodology for this study build on the phase velocity inversions of *Wagner et al*. [2010]. The model results presented here are the same as those in *Wagner et al*. [2013], but that paper focused exclusively on the interpretation of anisotropy beneath the Cascade arc. Here we expand our interpretation of this model to include a detailed analysis of areas east of the Cascade arc, and we include a number of new resolution tests to investigate the robustness of our surface wave phase velocity anisotropy results. To summarize our inversion methodology briefly, the inversions shown here analyze Rayleigh wave phase delays and amplitudes to determine the spatial variability of anisotropy directions and magnitudes in addition to velocity deviations for 12 periods between 33 and 143 s. We use data from 99 events of magnitude 6.3 or greater recorded at TA and HLP seismic stations (see *Wagner et al*. [2010] for data details). As described in *Wagner et al*. [2013], we use different grid node spacing for velocity and anisotropy terms. For velocity gridnodes, we use a spacing of 0.35°, and for anisotropy gridnodes, we use a broader spacing of 0.66°. Outermost gridnodes are left underdamped in order to "absorb" travel-time variations from outside the array that are not adequately modeled with our two-plane-wave approximation. We use the two-plane-wave method of *Forsyth and Li* [2005]. This method accounts for scattering by solving for the best fitting two plane waves that constructively and destructively interfere across the study area. For each plane wave, we solve for amplitude, phase, and back azimuth. Once the six plane wave parameters have been determined, we calculate the difference between predicted and observed amplitude and phase at each station. When calculating our predicted values, we incorporate the finite frequency kernels of *Zhou et al*. [2004] according to the method of *Yang and Forsyth* [2006]. The same sensitivity kernels are used for the newly added anisotropy terms. Phase velocities at any location are approximated by

$$C(\omega,\theta) = B_0(\omega) + B_1(\omega)cos(2\theta) + B_2(\omega)sin(2\theta)$$

omitting the higher-order $4\theta$ terms [e.g., *Smith and Dahlen*, 1973; *Weeraratne et al*., 2007]. The peak-to-peak strength of anisotropy is calculated as $2^*(B_1^2 + B_2^2)^{1/2}$ and the fast propagation direction is given by $0.5^*\arctan(B_2/B_1)$. Our preferred model is shown in Figure 4, and in supporting information, Figures S1–S3.

## 2.3. Resolution Tests for Rayleigh Wave Phase Velocity Anisotropy Results

[11] Here we assess our ability to resolve the anisotropy parameters in our inversion. To first order, it is possible to differentiate better-resolved areas from less well-resolved areas by plotting the standard deviations determined in the inversion for $B_1$ and $B_2$. Errors are propagated to fast direction azimuth and anisotropic strength. The standard deviations in anisotropic strength are much smaller than uncertainties derived from changes in regularization (see section 2.3.1), so we focus on errors in fast direction azimuth here. These are plotted for our preferred model in supporting information, Figure S1, for each period. Errors in fast direction are largest at the margins of our study area and are also large for measurements where the magnitude of anisotropy is very close to zero. We also plot the sum of the diagonal values of the resolution (R) matrix for each anisotropy grid node to indicate the degree to which model parameters trade off with those at adjacent grid nodes. Both the standard deviations and the R-matrix diagonals indicate that the best resolved areas are those in the center of our study area, particularly near the HLP seismic deployment where we have our greatest station density. Also well resolved are areas along the Cascade arc, the Owyhee Plateau, and along the Snake River Plain. At the longest periods, uncertainties are larger, consistent with decreased R-matrix diagonal values. This is due to the breadth of the finite frequency sensitivity kernels at long periods, which tend to blur any abrupt changes in velocity or anisotropy.

### 2.3.1. Regularization

[12] The results of any inversion are sensitive to the regularization used. In our inversions, regularization is accomplished by applying an a priori model covariance matrix to minimize the effects of small eigenvalues on the stability of the inversion. Our preferred model uses an a priori model

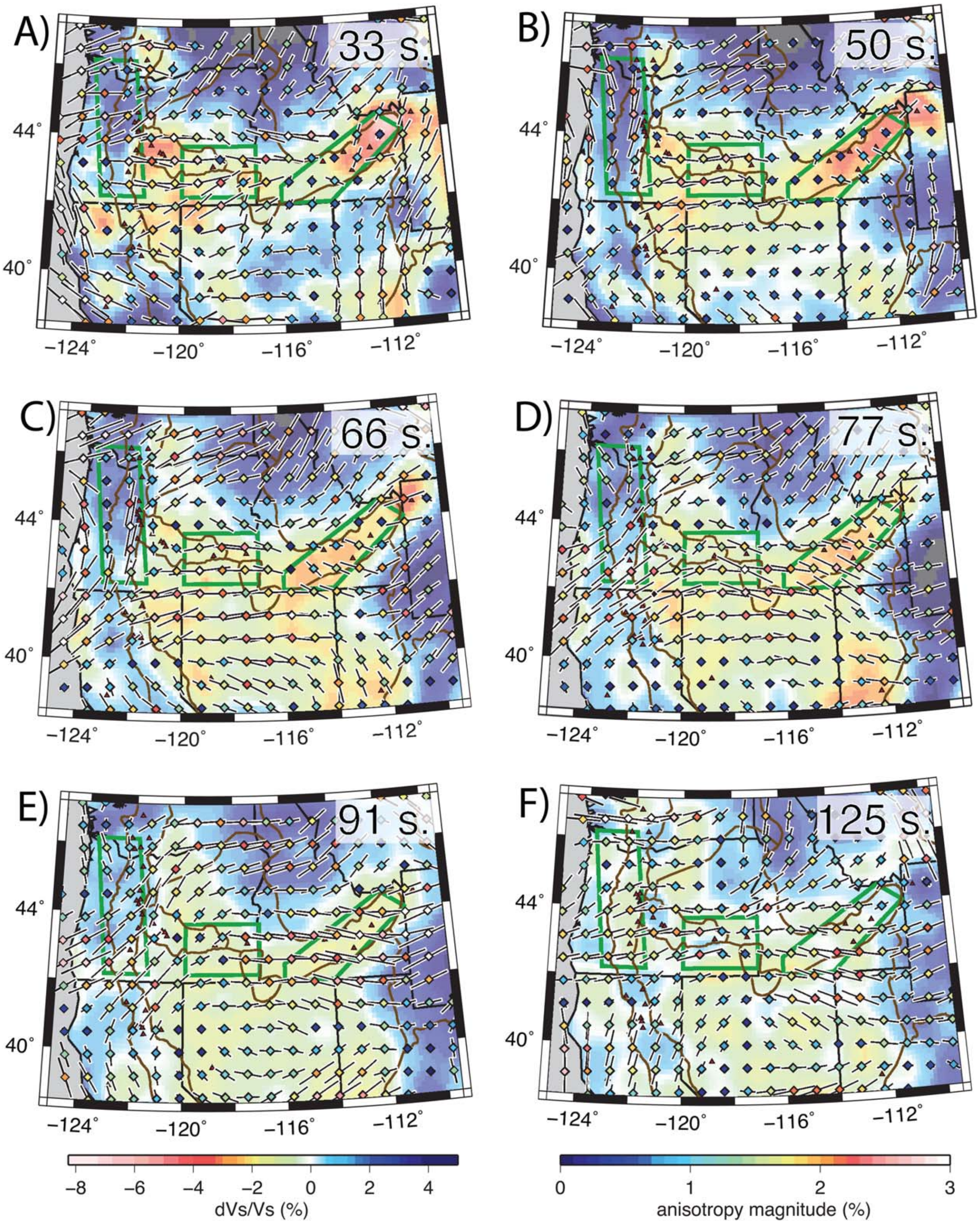

**Figure 4.** Results of Rayleigh wave phase velocity inversions with anisotropy parameters. Background colors indicate deviations from starting phase velocities at (a) 33 s, (b) 50 s, (c) 66 s, (d) 77 s, (e) 91 s, and (f) 125 s. Fast directions are shown by the directions of the black bars. The magnitude of anisotropy is denoted both by the color of the diamond at each node and by the length of the black bar. State boundaries are shown, as are the tectonic provinces shown in Figure 1. Green boxes indicate the bounds of the anisotropic areas described in section 2.3.1 and Figure 5.

covariance of 0.2 km/s for velocity parameters (consistent with *Wagner et al*. [2012a] and 0.04 for anisotropy parameters. We assess the effect of different covariance values on our anisotropy parameters in supporting information, Figure S2. Here we show the results of inversions that differ only in the covariance values applied to anisotropy parameters. Our results indicate that changes in regularization have little effect on fast direction, even in our less well-resolved areas. However, decreased covariance values for anisotropy terms result in strongly reduced peak-to-peak anisotropy magnitudes. Broadly speaking, increased covariances increase the apparent strength of anisotropy, especially at the edges of our study area where resolution is poor. However, in well-resolved areas, this increase in apparent anisotropy degree is not without limit. For example, within the bounds of the HLP seismic network where our resolution is strongest, anisotropic strength increases with increased covariance only up to our preferred covariance of 0.04. Further increases of covariance do not produce substantially increased apparent anisotropic strength, suggesting that some constraint on the maximum observed anisotropy is possible in well-resolved areas.

[13] To further test this hypothesis, we perform a regionalized inversion where anisotropy terms are assessed by region [*Li et al*., 2003]. This inversion assigns anisotropy terms to each velocity grid node and then combines the anisotropy sensitivities of all nodes within user-specified areas. This results in a single pair of anisotropy model parameters per area. We define one area that comprises much of the HLP where the largest shear wave splits are located, one area along the Cascade Arc, one area that encompasses the Snake River Plain, and finally we combine all other areas into a single pair of "Background" anisotropy terms. The three distinct areas are shown in Figures 3 and 4 and supporting information Figure S1. By reducing the number of anisotropy terms in the inversion, we are able to effectively remove the regularization applied to these terms by increasing their respective covariances to 1000. The results of these inversions are shown in Figure 5 and represent effectively undamped anisotropy values for these areas. These results are very consistent with the results of our preferred inversions for both the three defined areas and the background anisotropy, and are further discussed in section 3.

### 2.3.2. Starting model

[14] The robustness of our inversions can also be assessed by investigating the sensitivity of our results to the starting values assigned to anisotropy terms. Our preferred model has no starting anisotropy value assigned. To this end, we performed additional inversions in which we assigned starting anisotropy parameters equivalent to strong (5%) anisotropy with (1) E-W and (2) N-S fast directions. The results of these inversions were presented in *Wagner et al*. [2013] but were discussed only in the context of the Cascade arc. Here, we directly compare the results of these inversions with our preferred model in all areas, focusing on those areas east of the Cascade arc. In supporting information Figure S3, we plot the results of our preferred model compared to the results of the E-W starting anisotropy model and the N-S starting anisotropy model. Areas where our results are best resolved are those where these differences in both direction and magnitude are smallest. In general,

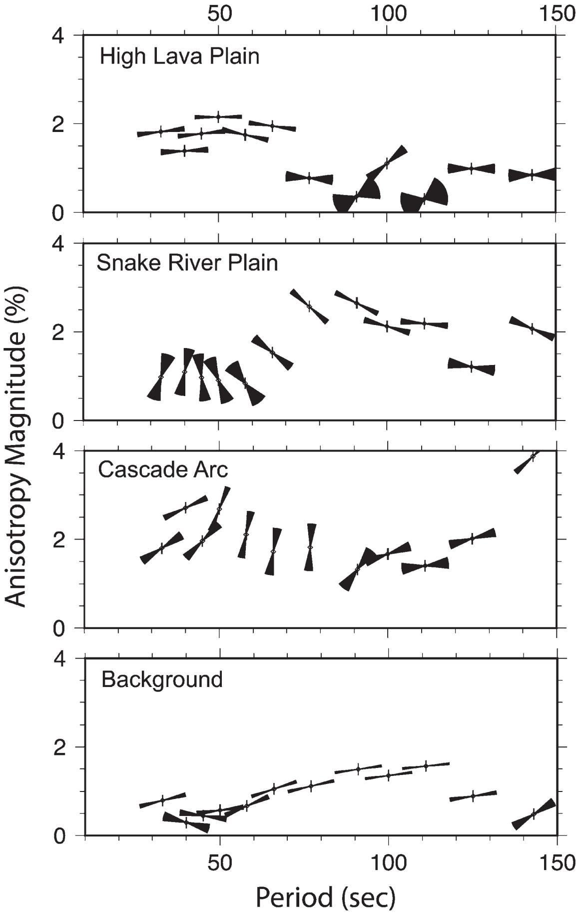

**Figure 5.** Results of inversions for regional anisotropy values, for the High Lava Plains, Snake River Plain, Cascade Arc, and "background" regions of the inversion. We plot the amplitude ($y$ axis) and direction (wedges, which show fast direction of phase velocities in map view with $2\sigma$ errors) of anisotropy as a function of period ($x$ axis). Vertical bars indicate error bars for magnitude (also $2\sigma$).

as with all other resolution tests performed, the edges of our study area are less robust than the central areas of our study area. In particular, the corners of the study area and areas in central Nevada, northern Idaho, and southern Washington show greater sensitivity to starting model. This is particularly true at longer periods. However, within the HLP and SRP, our resolution is very robust. In particular, we note that in the HLP, when the starting model included a 5% E-W trending anisotropy, the azimuth was not changed, but the magnitude of the anisotropy was reduced to the same value attained in our preferred model. Overall, these tests suggest that the direction of anisotropy in our preferred model is relatively insensitive to the starting model, at least for the well-resolved areas, and beneath the HLP in particular, the anisotropy magnitude is also not sensitive to the starting model.

## 3. Results

### 3.1. Large-Scale Anisotropy in the PNW

[15] In order to visualize large-scale patterns of SKS splitting beneath our PNW study area and compare these patterns with the Rayleigh wave anisotropy, we combine our SKS splitting data set with the measurements of *Schutt et al*. [1998] and *Fouch and West* [2008]. Figure 3 shows single-station average splitting parameters from these two studies along with our own HLP measurements. In the eastern part of our study area, fast splitting directions trend roughly parallel to the absolute motion of the North American plate (APM), while in eastern Oregon, the fast directions are generally E-W, with large splitting delay times (up to ~2.7 s). The semicircular pattern of fast directions in northern Nevada visible in the long-period surface wave phase velocities is also evident from the SKS splitting patterns [*West et al*., 2009]. We have previously interpreted the transition from E-W $\phi$ beneath eastern Oregon to APM-parallel $\phi$ beneath Idaho as being due to a transition from mantle flow controlled by slab rollback [*Druken et al*., 2011] to APM-parallel shear in the asthenosphere to the west [*Long et al*., 2012]. Superimposed on this general pattern, however, we see evidence from both SKS splitting and surface wave dispersion for pronounced variations in anisotropic strength and geometry (both laterally and with depth) beneath the HLP and SRP, as discussed below.

[16] Figure 4 presents our surface wave model results for 33, 50, 66, 77, 91, and 125 s. The isotropic velocity deviations from these inversions are almost identical to those from *Wagner et al*. [2010], where we solved only for the best fitting anisotropic fast direction and amplitude for the entire study area at a given period. Therefore, we do not discuss the isotropic phase velocities any further in this study; a complete discussion of these results can be found in *Wagner et al*. [2010, 2012a]. We focus instead on the new 2-D anisotropy results at each period. Notable features in our results include a sharp rotation from trench parallel to trench perpendicular fast directions for periods between 45 and 66 s beneath the Cascade arc, as discussed in *Wagner et al*. [2013]. We also see a broad-scale rotation at longer periods (>77 s) centered about central Nevada, consistent with the SKS splitting results of *Zandt and Humphreys* [2008] and *West et al*. [2009].

### 3.2. Anisotropy Beneath the HLP

[17] SKS splitting beneath the HLP exhibits relatively uniform fast directions (generally nearly E-W), but striking lateral variations in delay times. The dense station spacing of the HLP broadband experiment allows us to robustly characterize these variations, which are visible in map view in Figure 3. We observe a region of southeastern Oregon that is associated with large delay times (consistently $> 2$ s, with stations in the central part of the region exhibiting $\delta t > 2.5$ s), considerably larger than the surrounding region. This region coincides geographically with Holocene basalt flows, particularly Diamond and Jordan Craters. To the east of this region, stations located on the Owyhee Plateau exhibit smaller (~1.5–2 s) delay times. Delay times also decrease to the northwest along the HLP volcanic track toward Newberry, with average delay times less than 1.5 s. Similarly, delay times are reduced to the north of the HLP, with measured $\delta t$ as small as 1 s.

[18] Because of the dense station spacing of the HLP experiment, we are able to detect subtle changes in SKS fast direction and delay times within the footprint of the array, in addition to the broad-scale patterns. These changes are shown in Figure 6, which shows the single-station average $\varphi$ and $\delta t$ values as a function of distance along the NW-SE profile shown in Figure 3. This figure was constructed by "collapsing" all HLP stations located within 60 km of the profile (to the northeast) or 20 km of the profile (to the southwest) onto the profile line, and it reveals some interesting features. Starting in the northwest, delay times to the

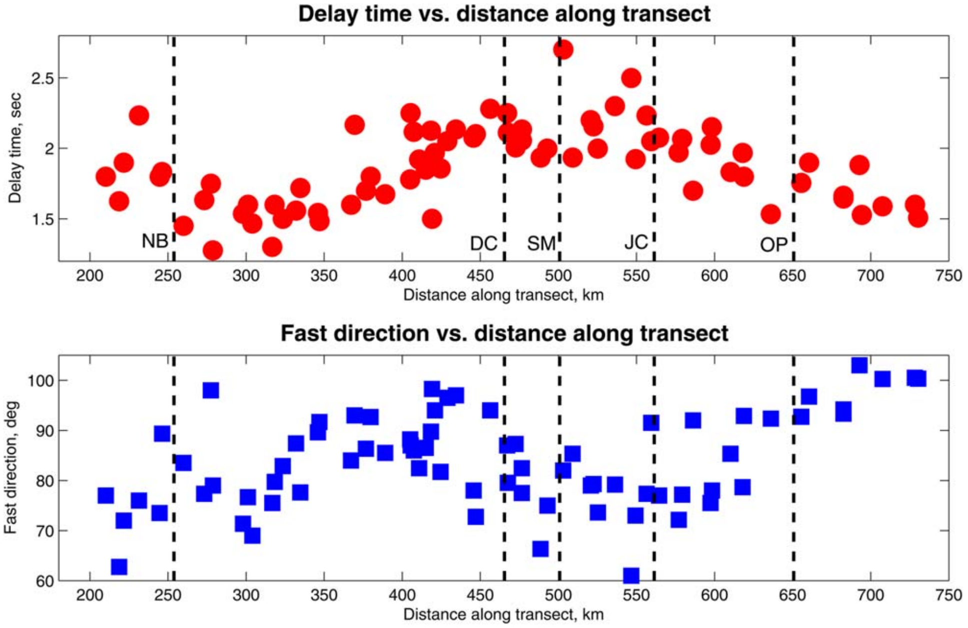

**Figure 6.** Variation of single-station average shear wave splitting delay times (top) and fast directions (bottom) along a NW-SE directed profile along the strike of the HLP trend. The profile is the same as that shown in Figure 3, although the ends of the profile have been truncated here to focus on the region with dense station coverage. All stations (from the HLP and TA arrays) located within 60 km of the profile (to the northeast) or 20 km of the profile (to the southwest) are shown. Average single-station parameters are the same as shown in Figure 3. Major geographic features are marked with a dashed line and initials: Newberry Volcano (NB), Diamond Craters (DC), Steens Mountain (SM), Jordan Craters (JC), and Owyhee Plateau (OP).

west of Newberry Volcano average nearly 2 s, but there is a pronounced drop in $\delta t$ just to the southeast of Newberry, to values less than 1.5 s. Continuing along the transect, $\delta t$ values climb steadily and then reach a plateau that has an average value greater than 2 s; the plateau covers the region between the Holocene basalt flows at Jordan Craters and Diamond Craters. To the southeast of Jordan Craters, delay times steadily decrease again to an average value of $\sim$1.7 s beneath the Owyhee Plateau. Some patterns in measured fast directions are also noticeable, although the vast majority of measured $\varphi$ values fall between 70° and 90° east of north. In the vicinity of Newberry, fast directions average approximately 80°; there is a slight rotation to a more nearly E-W direction in the vicinity of Diamond Craters, and then another slight rotation to $\varphi$ values near 70°–80° near Jordan Craters. To the southeast of Jordan Craters, there is a progressive clockwise rotation in fast directions to values just above 100° beneath the Owyhee Plateau.

[19] Beneath the HLP and the surrounding region, Rayleigh wave anisotropy also follows a relatively simple pattern, with fast directions varying slightly between E-W to ENE-WSW at all periods. The one exception is at 77 s where the easternmost part of Oregon shows a slight ESE-WNW fast direction. The magnitude of this anisotropy varies spatially and by period, but generally ranges from nearly zero up to 3% in our preferred model. While the magnitude of anisotropy is often very sensitive to starting model and regularization, we note that the magnitudes in southeastern Oregon remain remarkably consistent regardless of starting model (supporting information, Figure S3). Varying the regularization does affect magnitude, but in a predictable fashion, and not without limit (supporting information, Figure S2). In the very overdamped case, we note that the pattern of E-W fast directions is visible even though most of the surrounding area shows no anisotropy. As the initial covariance is increased, the magnitudes of anisotropy in southeastern Oregon increase. However, once the covariance reaches 0.04 and above, magnitudes cease to increase with increasing covariance, attaining a maximum value <= 3%. The magnitude and direction of the anisotropy for covariance values of 0.04 and larger are consistent with the results of the undamped regionalized inversion for anisotropy parameters (Figure 5). These indicate consistently E-W fast directions except for 100 s period Rayleigh waves, which show an ENE-WSW fast direction. The anisotropy in these inversions

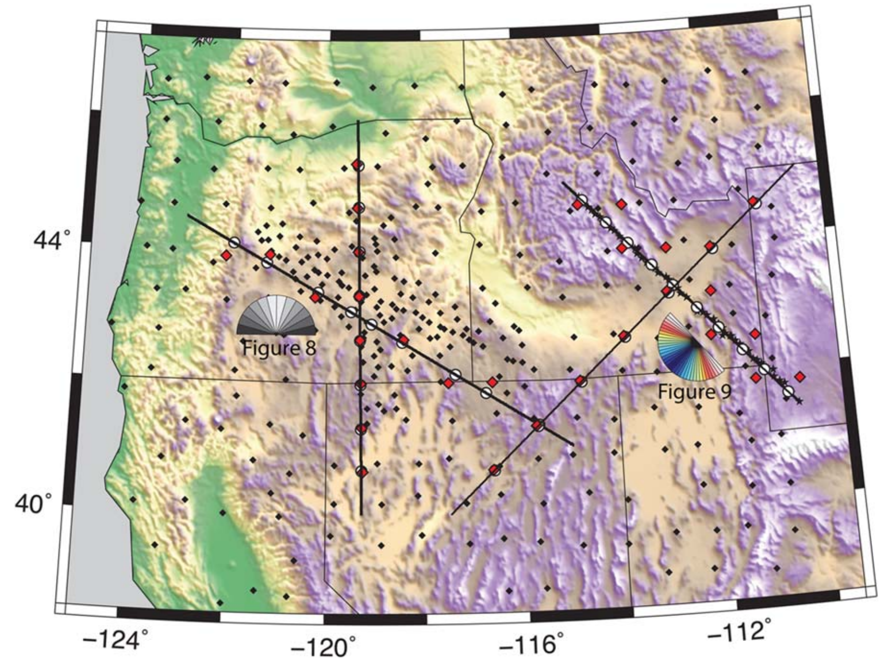

**Figure 7.** Map of cross sections. Background colors indicate topography. Red diamonds show anisotropy grid nodes displayed on cross sections in Figures 6–9. White circles show their projected location along the transect. Small black stars show the station locations in *Schutt et al*. [1998]. Black diamonds show station locations. Fan of black-white color scale in Oregon shows colors used to plot surface wave kernels in Figures 6 and 7 (degrees from north). Fan of rainbow color scale in Idaho shows colors used to plot surface wave kernels in Figures 8 and 9 (degrees from absolute plate motion).

is strongest (~2%) at periods of between 33 and 66 s, decreasing to ~0.5–1% for longer periods. All of these tests combined strongly suggest that the maximum value of Rayleigh wave anisotropy observed at any one period across southeastern Oregon does not exceed 3%, and is likely more on the order of 1–2%.

[20] The lateral variability of anisotropy in and near the HLP is particularly evident in cross section. Figure 7 shows the locations of cross sections, and Figure 8 shows fast directions and magnitudes of anisotropy at grid nodes adjacent to the transects represented by color and line weight, respectively. Also plotted are SKS splitting delay times and fast directions. Figure 8a is oriented roughly parallel to the track of HLP post-Miocene volcanism. Figure 8b shows a North-South transect close to the dense N-S seismic line of the HLP broadband experiment. We observe very strong E-W trending anisotropy, along with large SKS splitting delay times, directly beneath the High Lava Plains regions, particularly in areas characterized by very low lower crustal/uppermost mantle velocities. Closer to the subducting Juan de Fuca slab (Figure 8a), we see the sharp rotation to N-S fast directions associated with the presence of hydrous phases [*Wagner et al*., 2013], and moderate E-W fast directions beneath the arc just west of the HLP. Within the HLP, the E-W trending anisotropy is particularly strong at shorter periods that are sensitive to shallower depths. At the southeastern end of the diagonal transect, we see much weaker anisotropy and somewhat more variable fast directions, especially at periods sampling the higher velocity crust and mantle lithosphere associated with the Owyhee Plateau. In the North-South transect (Figure 8b), we see anisotropy that is notably weaker north and south of the low velocities associated with the HLP, consistent with decreases in observed SKS splitting times.

### 3.3. Anisotropy Beneath the SRP

[21] Rayleigh wave anisotropy results across central and northern Idaho indicate fast directions approximately parallel to North American plate motion north of the SRP (Figures 1 and 4). Within the SRP, however, we observe very weak anisotropy oriented obliquely to APM at periods shorter than 77 s. At longer periods, we observe stronger anisotropy more closely aligned to APM. This is consistent with our regionalized inversions (Figure 5) that show very weak N-S oriented fast

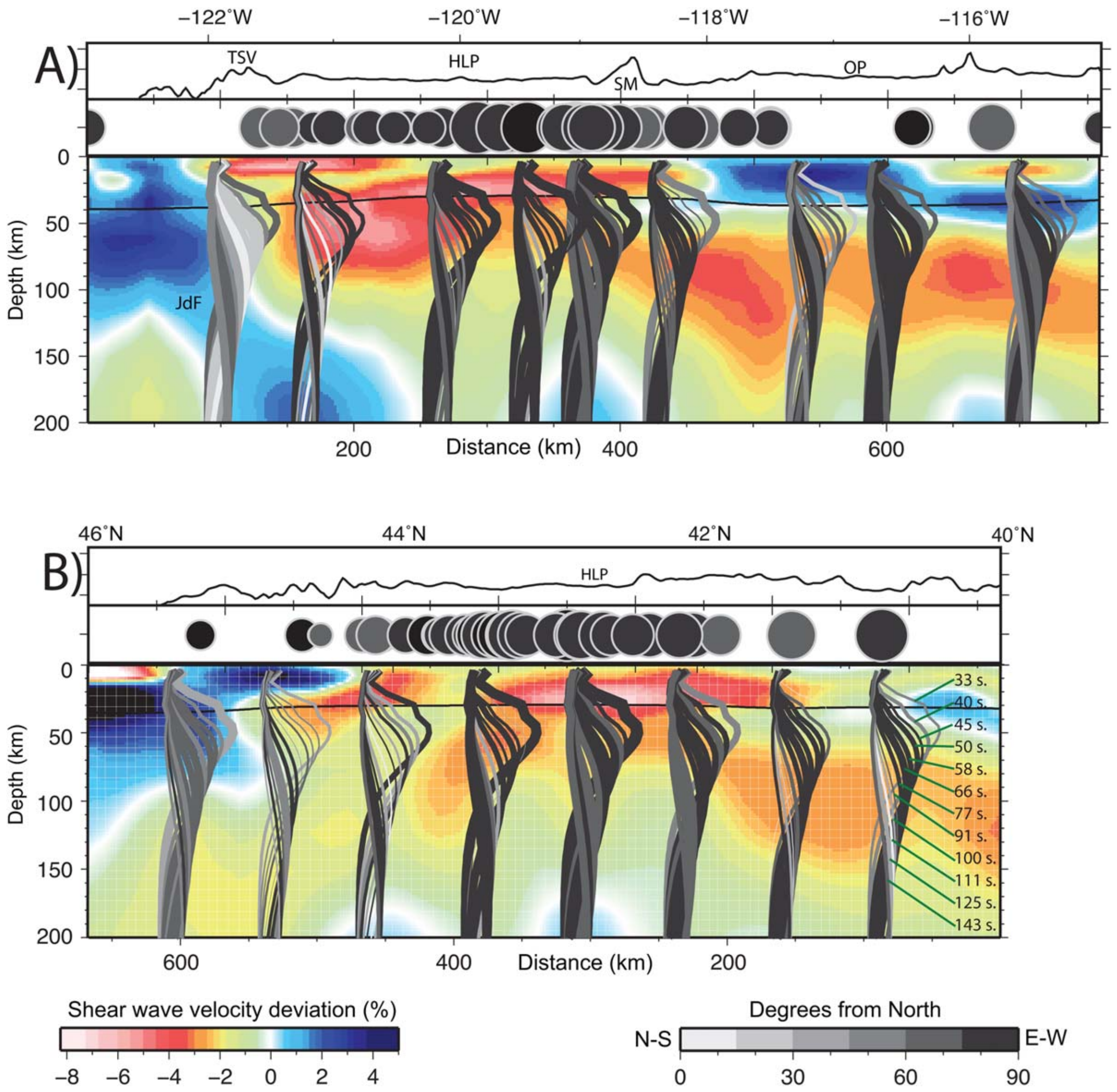

**Figure 8.** Cross section of Rayleigh wave inversion results diagonally across (a) the HLP and (b) along a north-south transect across the HLP. Background is from the shear wave velocity model of *Wagner et al.* [2012a]. Black and gray lines are the sensitivity kernels for periods from 33 to 143 s. The line weight is scaled according to the magnitude of anisotropy at that period at the grid node closest to that location on the cross section (see Figure 7 for grid nodes and projection locations). The color of the kernel lines indicates degrees from due North (white = North-South; black = East-West). Circles above the cross section show projected SKS splits for stations within 30 km of the transect (Figure 3). The size of the circle represents delay time and the grayscale indicates degrees from north. Black lines above the circles show the regional topography along the profile. Labeled features are as follows: SM = Steens Mountain; TSV = Three Sisters Volcanoes; JdF = Juan de Fuca Slab; HLP = High Lava Plain; OP = Owyhee Plateau.

directions for periods between 33 and 66 s, and much stronger, more E-W oriented fast directions at periods of 77 s and longer.

[22] To examine the spatial extent of this pattern, we plot cross sections along and orthogonal to the Snake River Plain and project our anisotropy results onto these cross sections (Figure 9). Here, the sensitivity kernels of each period for a given anisotropy node are color coded according to the degree different from APM, as opposed to the color coding in Figure 8 which is relative to direction from north. We have used different color scales to emphasize the difference. Both color scales can be seen in Figure 7. The alongstrike profile (Figure 9a) shows a distinctly different pattern of anisotropy in the central portion of the SRP

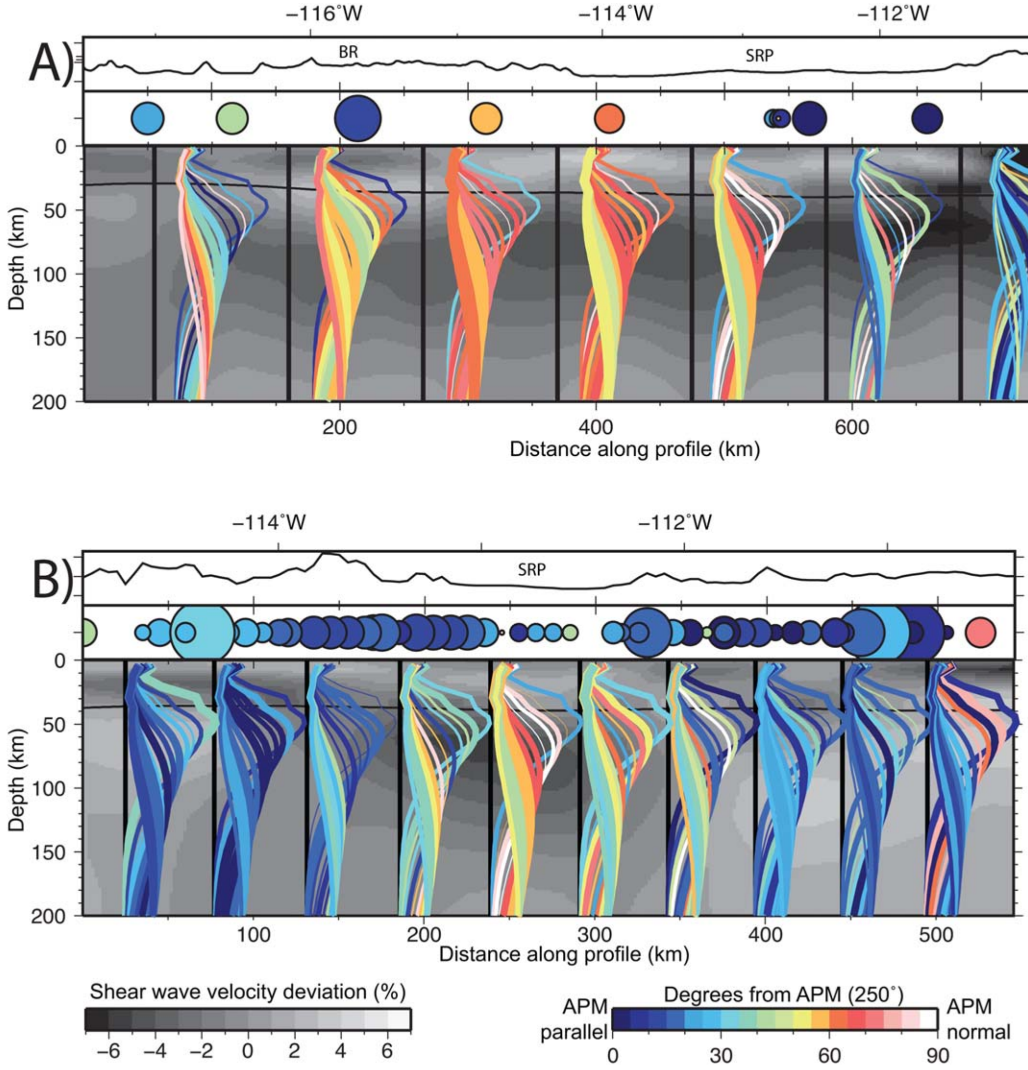

**Figure 9.** Cross section of Rayleigh wave inversion results along the strike of (a) the SRP and (b) perpendicular to strike. Lines are sensitivity kernels whose line weight is proportional to the magnitude of anisotropy, as described for Figure 8. Color scale is degrees from absolute plate motion (see Figure 7 for color scale). The color palette differs from that in Figure 8 to emphasize the difference in the reference azimuth (north-south in Figure 8 versus APM in Figure 9). Grayscale background shows the shear wave velocity model from *Wagner et al*. [2012a]. Circles above the cross section show projected SKS splits for stations within 30 km of the transect (Figure 3). The size of the circle represents delay time and the color indicates degrees from absolute plate motion. Black lines above the circles show the regional topography along the profile. Labeled features are as follows: SRP = Snake River Plain, BR = Basin and Range; Y = Yellowstone.

than beneath Yellowstone, where APM-parallel fast directions are observed at all periods. The cross section orthogonal to the trend of the SRP shows that the pattern of small, APM-oblique fast directions at short periods and stronger APM-subparallel fast directions at longer periods is observed directly below the SRP but not in areas further to the north and south. We compare our results to the shear wave splitting results of *Schutt et al*. [1998]. They find very small SKS splitting times within the SRP, but much stronger, APM parallel shear wave splitting to the north and south. This would be consistent with the presence of deeper APM parallel flow that is canceled out by shallower, APM-oblique fast directions. Later work by *Waite et al*. [2005] examined stations to the north and east of the transect investigated by *Schutt et al*. [1998], and found no evidence for smaller SKS splitting values within the SRP. This is consistent with our Rayleigh wave anisotropy results that show this pattern constrained to the central portion of the Snake River Plain.

# 4. Discussion

## 4.1. Comparison Between SKS and Surface Wave Models

[23] In general, the patterns of upper mantle anisotropy that we infer from our SKS splitting and surface wave models agree well (Figures 3 and 4). However, there is a discrepancy in the magnitude of the anisotropy beneath the HLP inferred from the different types of observations. Our observation of SKS splitting delay times that exceed 2 s in southeastern Oregon suggests strong anisotropy in the asthenospheric upper mantle. If the anisotropy is confined to a layer of ∼150 km thick in the asthenosphere, then an anisotropic strength of ∼6–8% is required, even if some of the delay time is accounted for via anisotropy in the lithosphere [see also *Long et al*., 2009]. While a large delay time could be accrued if there is a substantial contribution from the deeper parts of the upper mantle [e.g., *Yuan and Romanowicz*, 2010], the observation of variations in delay time of ∼1–1.5 s over relatively short length scales (a few hundred kilometers; Figures 3 and 6) argues for the most substantial contribution coming from the shallow part of the upper mantle.

[24] The high magnitude of upper mantle anisotropy suggested by the SKS splitting times is not observed in the anisotropic model derived from Rayleigh waves. We consistently find a maximum anisotropy of <4%, usually <2.5%. This encompasses all periods with maximum sensitivities between 40 and 150 km depth, and with longer periods still sensitive to depths of up to 250 km. It is highly unlikely that structures shallower than 40 km, to which our surface wave data are less sensitive, can explain the discrepancy. *Long et al*. [2009] suggested that the high delay times beneath the HLP would require 20% anisotropy over a 60 km thick layer of the lithosphere, assuming no asthenospheric contribution. Such strong anisotropy, especially in the lower crust, would have strongly affected the 33 and 40 s Rayleigh waves, which we do not observe. It is possible that a substantial portion of the observed anisotropy is sourced at depths below the sensitivity of our surface waves. Again, however, the SKS delay time observations vary over short spatial scales, suggesting a relatively shallow source.

[25] The amplitude discrepancy between observed SKS splitting times and anisotropy inferred from anisotropic surface wave tomography has been noted before [e.g., *Becker et al*., 2012]. The difference could be artifacts of tomographic smoothing or overestimation of delay times from noisy SKS phases [e.g., *Monteiller and Chevrot*, 2009], but all of these issues are much mitigated with a small study area and a dense and high-quality SKS data set, such as the one presented here. We have investigated the effects of regularization in the surface wave inversion, and see no evidence for much anisotropy greater than 3% across central and southeastern Oregon. While the resolution of this discrepancy is beyond the scope of this paper, we suggest that southeastern Oregon may be an ideal locale to further study this phenomenon, given the simplicity of the anisotropy, the magnitude of the SKS delay times, and the extremely dense but laterally broad seismic data coverage afforded by the combination of the High Lava Plains deployment and the EarthScope Transportable Array.

## 4.2. Comparison With Previous Work

[26] It is also instructive to compare our inferences on upper mantle anisotropy beneath the PNW to previous studies. Our SKS splitting data set beneath the HLP is very consistent with previous work [*Xue and Allen*, 2006], although the very dense station spacing provided by the HLP broadband experiment allows us to constrain lateral variations in delay time in greater detail. Complementary constraints on the geometry and strength of uppermost mantle anisotropy can be obtained from anisotropic Pn analysis, either through tomography or localized imaging techniques. *Buehler and Shearer* [2012] identify patterns of Pn anisotropy that are generally consistent with what we infer, including a region of generally trench-parallel fast anisotropic directions beneath the Cascades [*Wagner et al*., 2013] and generally E-W fast directions beneath the HLP with an anisotropy strength up to ∼8%. We can also compare our results with other models for azimuthal anisotropy beneath the PNW that use both SKS splitting and surface wave observations, notably those of *Yuan and Romanowicz* [2010] and *Lin et al*. [2011]. To first order, our inferences agree with the features observed in these models, sometimes in relatively fine detail. For example, there are strong similarities between the well-resolved portions of our anisotropic phase velocity map at 33 s and that of *Lin et al*. [2011] at 38 s. However, we also observe some differences in fine-scale details with previous models. For example, the model of *Yuan and Romanowicz* [2010] resolves several layers of anisotropy beneath the HLP, with NE-SW fast directions at shallower depths (∼70–100

km) and a transition to NW-SE fast directions in the deeper upper mantle (~200–300 km). This is in contrast to the relatively uniform E-W fast directions throughout the upper mantle beneath the HLP that we infer from surface waves (Figure 8a) and from the lack of backazimuthal variation in apparent SKS splitting parameters (Figure 2).

## 4.3. Possible Mechanisms for the Anomalous Anisotropy

[27] Our inference of anomalous anisotropy beneath both the HLP and SRP suggests that there is a modification to the mechanism of anisotropy beneath both of these active volcanic tracks, compared to the surrounding regions. However, the distinctive anisotropy takes different forms: beneath the HLP, we observe a region of particularly strong anisotropy beneath southeastern Oregon, while the magnitude lessens to the northwest as the HLP rhyolites get younger (Figure 8a). Beneath the SRP, in contrast, there is an anomaly in the geometry, rather than the magnitude, of anisotropy, and there is an excellent spatial correlation between the anomalous anisotropy and particularly low isotropic wavespeeds along much of the SRP. Interestingly, for both the SRP and the HLP, we do not observe anomalous anisotropy beneath the youngest part of the (rhyolitic) volcanic tracks. Beneath the northwestern end of the HLP track in the vicinity of Newberry volcano, the SKS splitting delay times are modest and the Rayleigh wave anisotropy is not particularly strong (Figure 8a). Similarly, beneath the eastern end of the SRP track near Yellowstone, we do not observe a striking change in the anisotropic geometry with depth (Figure 9).

[28] We have considered a number of models to explain the lateral variations in upper mantle anisotropy beneath the HLP and SRP. To consider the HLP case first, we seek a model that can explain a large variability in SKS delay times and Rayleigh anisotropy strength in the context of the very simple E-W asthenospheric flow field beneath the HLP that has been inferred from geodynamical experiments [*Druken et al*., 2011; *Long et al*., 2012]. There are a few scenarios that can be ruled out relatively easily. Specifically, variations in crustal anisotropy or anisotropy in the shallow mantle lithosphere are unlikely, as the strength of crustal anisotropy would have to be unreasonably large (up to ~30%) to explain the delay time observations. Additionally, receiver function studies of crustal structure beneath the HLP do not find evidence for strong crustal anisotropy [*Eagar et al*., 2011]. We also do not expect dramatic small-scale lateral variations in the thickness of the anisotropic asthenospheric layer or in the amount of strain accumulated in the upper mantle, based mainly on geodynamical modeling constraints [*Druken et al*., 2011]. However, we have identified three plausible models for the lateral variations in anisotropy strength we observe beneath the HLP: (1) variations in olivine LPO strength as a consequence of changing deformation conditions (temperature, stress, water), (2) variations in olivine fabric type as a consequence of changing deformation conditions, and (3) variations in the amount and/or alignment of partial melt in the upper mantle beneath the HLP.

[29] There is a large amount of variability in the strength of olivine LPO (and thus shear wave anisotropy) in natural peridotite rocks, from nearly isotropic up to ~15% [*Ben Ismail and Mainprice*, 1998; *Mainprice*, 2007]. The strength of olivine LPO can be measured quantitatively through a measure such as the M-index [*Skemer et al*., 2005] and may be influenced by many factors, such as the history [e.g., *Skemer et al*., 2012] and conditions of deformation, perhaps including the temperature, water content, strain rate, grain size, mineralogy, and presence or absence of partial melt [e.g., *Kaminski et al*., 2004; *Skemer et al*., 2010; *Falus et al*., 2011]. Fabric strength does not appear to be strongly influenced by the amount of strain in natural rocks [e.g., *Warren et al*., 2008]. Unfortunately, many of the variables that may affect the strength of olivine LPO are poorly constrained for the upper mantle beneath the HLP. Inferences on the temperature conditions may be gleaned from the interpretation of tomography models and from the petrological characteristics of volcanic rocks. *Till et al*. [2013] inferred uppermost mantle temperatures of 1185–1383°C beneath the HLP from basalt thermometry, with generally hotter temperatures beneath southeastern Oregon (Diamond and Jordan Craters) and generally cooler temperatures beneath Newberry volcano, suggesting lateral some variations in temperature. Lateral temperature variations in the upper mantle are also suggested by isotropic surface wave tomography [*Wagner et al*., 2010, 2012a], although a straightforward thermal interpretation of the models would suggest particularly high temperatures in the vicinity of Newberry. In any case, the effects of the many factors that may influence the strength of LPO (such as temperature) remain poorly constrained from a mineral physics point of view. Therefore, while lateral

variations in the strength of olivine LPO (due to temperature variations or other factors) remains a plausible mechanism to explain the variability in anisotropy strength beneath the HLP, this remains a difficult hypothesis to evaluate quantitatively.

[30] Another related hypothesis is that there is a transition in olivine fabric type beneath the HLP. It is likely that A-, C,- or E-type olivine fabric dominates in the relatively low-stress, high-temperature asthenospheric mantle, while D-type fabric may dominate in the lithospheric mantle and B-type fabric may be present in the high-stress, low-temperature corner of the subduction zone mantle wedge [e.g., *Karato et al*., 2008]. Fabric transitions in the upper mantle have been inferred from seismologic observations (for example, the transition to B-type fabric inferred by *Nakajima and Hasegawa* [2004] and *Kneller et al*. [2008]), from laboratory experiments [*Jung and Karato*, 2001; *Katayama et al*., 2004; *Jung et al*., 2006], and from natural rocks [*Wang et al*., 2013; *Precigout and Hirth*, 2011]. An intriguing possibility is that the particularly strong anisotropy we infer beneath southeastern Oregon represents a transition from A-type to E-type olivine fabric. While both of these fabric types is associated with a fast direction of anisotropy aligned in the direction of maximum finite strain, E-type fabric is associated with stronger azimuthal anisotropy than A-type fabric [*Karato*, 2008]. A transition from A-type to E-type fabric at high temperatures and modest stresses is associated with an increase in water content above ∼200 ppm [*Karato et al*., 2008]; it is not well known how temperature affects this transition. It is possible that lateral variations in water content or, perhaps, temperature beneath the HLP may induce a transition in olivine fabric type that leads to stronger anisotropy beneath southeastern Oregon even if the strain geometry is uniform. Further investigations of the effect of temperature on olivine fabric transitions and on the possibility of variations in upper mantle water content beneath the HLP may allow further quantitative testing of this hypothesis.

[31] A third plausible mechanism to explain the lateral variations in anisotropy beneath the HLP is a possible contribution from partial melt. Partial melt may modify the anisotropic structure of mantle rocks, either by modifying olivine LPO in the surrounding matrix [*Holtzman et al*., 2003; *Higgie and Tommasi*, 2012] or via a shape-preferred orientation effect [*Holtzman and Kendall*, 2010; *Tommasi et al*., 2006], although this effect can be difficult to assess quantitatively for the upper mantle because the melt fraction and topology are typically not well known [e.g., *Vauchez and Garrido*, 2001]. Previous seismologic studies have inferred a contribution to seismic anisotropy observations from partial melt in the context of mid-ocean ridge spreading or continental rifting [e.g., *Kendall*, 1994; *Bastow et al*., 2010; *Hammond et al*., 2010]. It is possible that the particularly high delay times we observe beneath southeastern Oregon are due to a melt shape preferred orientation (SPO) effect that constructively interferes with the background signal from olivine LPO, as the recent basaltic volcanism suggests that some degree of partial melt should be present beneath this region [*Till et al*., 2013]. However, it is not immediately obvious why such a mechanism would not also be operative beneath the northwestern part of the HLP, which has also experienced Holocene volcanism (Figure 1) but which exhibits smaller SKS delay times. As with the olivine LPO mechanisms, the large uncertainties about the partial melt fraction and alignment in the upper mantle, along with uncertainties about the effect of partial melt on anisotropy under different conditions of deformation, hamper our ability to quantitatively test the melt SPO hypothesis.

[32] There are several possible models that might explain the lateral variations in anisotropic strength beneath the HLP, but since the anomalous anisotropy beneath the SRP involves a change in geometry rather than strength, the mechanism must be different. The abrupt deviation from APM-parallel fast directions beneath the SRP is puzzling, as elsewhere in Idaho fast directions generally trend NE-SW and have been interpreted as being due to simple shear in the asthenosphere induced by North American plate motion [e.g., *Waite et al*., 2005; *Long et al*., 2012]. It is difficult to envision a mantle dynamics regime that would give rise to dominantly NE-SW finite strain directions throughout Idaho but would allow for finite strain directions roughly perpendicular to this directly beneath the SRP. Given the extremely low upper mantle wavespeeds beneath the SRP [e.g., *Wagner et al*., 2010, 2012a] and the high conductivity channel inferred from the inversion of magnetotelluric measurements [*Kelbert et al*., 2012], it is highly likely that partial melt is present beneath the SRP, likely with melt fractions up to 3% [*Kelbert et al*., 2012]. An intriguing possibility is that the deformation of the partially molten upper mantle beneath the SRP, either via APM-induced shear or from mantle flow along the Yellowstone hotspot

track driven by a mantle plume [e.g., *Camp and Ross*, 2004], is inducing a distinctive anisotropy with fast directions oriented at high angles (approaching 90°) to the flow direction within the partially molten, low-velocity, high-conductivity channel beneath much of the SRP. This anisotropy may take the form of melt SPO, if melt is aligned in sheets or tubules perpendicular to the strike of the SRP trend, or it may represent a modification of olivine fabric due to deformation in the presence of melt [*Holtzman et al.*, 2003; *Higgie and Tommasi*, 2012]. Further work is needed to determine whether the conditions of deformation beneath the SRP, particularly the ~3% melt fraction inferred from electromagnetic data, are indeed consistent with a scenario in which the fast directions of anisotropy are aligned at high angles to the prevailing mantle flow direction.

## 5. Summary

[33] We have investigated the anisotropic structure of the upper mantle beneath the Pacific Northwest, and beneath the High Lava Plains and Eastern Snake River Plain in particular, using a combination of SKS splitting analysis and Rayleigh wave dispersion analysis. Similar patterns of anisotropic fast directions are suggested by both types of observations, although the magnitude of anisotropy suggested by the SKS delay times is generally higher (by a factor of ~2) than that inferred from the surface waves. Beneath the HLP, we infer generally E-W fast directions with striking spatial variations in anisotropic strength. A region of particularly strong anisotropy beneath southeastern Oregon coincides spatially with the geographic location of Holocene volcanism. Possible mechanisms for the observed variations in anisotropic strength include variations in olivine fabric type, olivine LPO strength, or the amount or alignment of partial melt. Beneath most of the SRP, Rayleigh wave observations at periods suggest a rotation in the fast direction of anisotropy with depth compared to the surrounding mantle, although such a dramatic rotation is not observed directly beneath Yellowstone. We infer that there is a region of anisotropy beneath the SRP with dramatically different geometry than that of the surrounding mantle that appears to coincide with the channel of extremely low isotropic wavespeeds (at depths between ~50–120 km). A likely mechanism for this change in geometry is the effect of partial melt on the effective anisotropy. Both the HLP and SRP exhibit distinctive upper mantle anisotropy compared to the surrounding regions, although anomalous structure takes different forms (particularly strong anisotropy beneath the HLP and a rotation in fast direction beneath the SRP). Given the volcanic history of both the HLP and the SRP over the past ~12 Ma, it is likely that partial melt in the upper mantle plays a role in controlling the anisotropic structure, particularly beneath the SRP. Large uncertainties remain in our understanding of how the conditions of deformation and the amount of partial melt affect the strength and geometry of upper mantle anisotropy. We suggest, however, that the combined SKS and Rayleigh wave data set presented here, which documents distinctive and well-constrained variations (both laterally and with depth) in anisotropy beneath the HLP and SRP, could serve as a useful test for the ongoing development of quantitative models of olivine fabric transitions, LPO strength, and the effect of partial melt on anisotropic structure.

## Acknowledgments

[34] L.S.W. acknowledges support from NSF via grant EAR-0809192 and M.D.L. acknowledges support from an Alfred P. Sloan Research Fellowship. Data for this project came from the High Lava Plains seismic experiment, which was funded by the NSF Continental Dynamics program, and from the EarthScope USArray Transportable Array (TA). We are grateful to the PASSCAL and DMC programs of the Incorporated Research Institutions for Seismology (IRIS) for enabling the collection, archiving, and dissemination of these data. We thank the participants in the HLP Project effort for engaging scientific discussions, particularly Rick Carlson, Kelsey Druken, Matt Fouch, David James, Chris Kincaid, and Christy Till. We are grateful to two anonymous reviewers for constructive suggestions that helped to improve the manuscript.

## References

Armstrong, R. L., W. P. Leeman, and H. E. Malde (1975), K-Ar dating quaternary and neogene volcanic rocks of the Snake River Plain, Idaho, *Am. J. Sci.*, *275*, 225–251.

Bastow, I. D., S. Pilidou, J.-M. Kendall, and G. W. Stuart (2010), Melt-induced seismic anisotropy and magma assisted rifting in Ethiopia: Evidence from surface waves, *Geochem. Geophys. Geosyst.*, *11*, Q0AB05, doi:10.1029/2010GC003036.

Becker, T. W., S. Lebedev, and M. D. Long (2012), On the relationship between azimuthal anisotropy from shear wave splitting and surface wave tomography, *J. Geophys. Res.*, *117*, B01306, doi:10.1029/2011JB008705.

Ben Ismail, W., and D. Mainprice (1998), An olivine fabric database: An overview of upper mantle fabrics and seismic anisotropy, *Tectonophysics*, *296*, 145–158.

Buehler, J. S., and P. M. Shearer (2012), Localized imaging of the uppermost mantle with USArray Pn data, *J. Geophys. Res.*, *117*, B09305, doi:10.1029/2012JB009433.

Camp, V. E., and B. B. Hanan (2008), A plume-triggered delamination origin for the Columbia River Basalt Group, *Geosphere*, *4*, 480–495.

Camp, V. E., and M. E. Ross (2004), Mantle dynamics and genesis of mafic magmatism in the intermontane Pacific Northwest, *J. Geophys. Res. 109*, B08204, doi:10.1029/2003JB002838.

Carlson, R. W., and W. K. Hart (1987), Crustal genesis on the Oregon Plateau, *J. Geophys. Res.*, *92*, 6191–6206.

Carlson, R. W., D. E. James, M. J. Fouch, T. L. Grove, W. K. Hart, A. L. Grunder, R. A. Duncan, G. R. Keller, S. H. Harder, and C. R. Kincaid (2005), On the cause of voluminous magmatism in the northwestern United States, *Geol. Soc. Am. Abstr. Programs*, *37*, 125.

Cross, T. A., and R. H. Pilger (1978), Constraints on absolute motion and plate interaction inferred from Cenozoic igneous activity in the western United States, *Am. J. Sci.*, *278*, 865–902.

Darold, A., and E. Humphreys (2013), Upper mantle seismic structure beneath the Pacific Northwest: A plume-triggered delamination origin for the Columbia River flood basalt eruptions, *Earth Planet. Sci. Lett.*, *365*, 232–242.

Druken, K. A., M. D. Long, and C. Kincaid (2011), Patterns in seismic anisotropy driven by rollback subduction beneath the High Lava Plains, *Geophys. Res. Lett.*, *38*, L13310, doi:10.1029/2011GL047541.

Eakin, C. M., M. Obrebski, R. M. Allen, D. C. Boyarko, M. R. Brudzinski, and R. Porritt (2010), Seismic anisotropy beneath Cascadia and the Mendocino triple junction: Interaction of the subducting slab with mantle flow, *Earth Planet. Sci. Lett.*, *297*, 627–632, doi:10.1016/j.epsl.2010.07.015.

Eagar, K. C., M. J. Fouch, D. E. James, and R. W. Carlson (2011), Crustal structure beneath the High Lava Plains of eastern Oregon and surrounding regions from receiver function analysis, *J. Geophys. Res.*, *116*, B02313, doi:10.1029/2010JB007795.

Falus, G., A. Tommasi, and V. Soustelle (2011), The effect of dynamic recrystallization on olivine crystal preferred orientations in mantle xenoliths deformed under varied stress conditions, *J. Struct. Geol.*, *33*, 1528–1540.

Ford, M. T., A. L. Grunder, and R. A. Duncan (2013), Bimodal volcanism of the High Lava Plains and northwestern Basin and Range of Oregon: The distribution and tectonic implications of age-progressive rhyolites, *Geochem. Geophys. Geosyst.*, *14*, doi:10.1002/ggge.20175, in press.

Forsyth, D. W., and A. Li (2005), Array analysis of two-dimensional variations in surface-wave phase velocity and azimuthal anisotropy in the presence of multipathing interference, in *Seismic Earth: Array Analysis of Broadband Seismograms, AGU Geophys. Monogr. Ser*., vol. *157*, edited by A. Levander and G. Nolet, pp. 81–98, AGU, Washington, D. C.

Fouch, M. J., and J. D. West (2008), High resolution imaging of the mantle flow field beneath western North America, *Eos Trans. AGU*, *89*(53), Fall Meet. Suppl., Abstract U53C-06.

Gao, H., E. D. Humphreys, H. Yao, and R. D. van der Hilst (2011), Crust and lithosphere structure of the northwestern US with ambient noise tomography: Terrane accretion and Cascade arc development, *Earth Planet. Sci. Lett.*, *304*, 202–211.

Hales, T. C., D. L. Abt, E. D. Humphreys, and J. J. Roering (2005), A lithospheric instability origin for Columbia River flood basalts and Wallowa Mountains uplift in northeast Oregon, *Nature*, *438*, 824–845.

Hammond, J. O. S., J.-M. Kendall, D. Angus, and J. Wookey (2010), Interpreting spatial variations in anisotropy: Insights into the Main Ethiopian Rift from SKS waveform modeling, *Geophys. J. Int.*, *181*, 1701–1712.

Hanson-Hedgcock, S., L. S. Wagner, M. J. Fouch, and D. E. James (2012), Constraints on the causes of mid-Miocene volcanism in the Pacific Northwest US from ambient noise tomography, *Geophys. Res. Lett.*, *39*, L05301, doi:10.1029/2012GL051108.

Higgie, K., and A. Tommasi (2012), Feedbacks between deformation and melt distribution in the crust-mantle transition zone of the Oman ophiolite, *Earth Planet. Sci. Lett.*, *359-360*, 61–72.

Holtzman, B. K., and J.-M. Kendall (2010), Organized melt, seismic anisotropy, and plate boundary lubrication, *Geochem. Geophys. Geosyst.*, *11*, Q0AB06, doi:10.1029/2010GC003296.

Holtzman, B. K., D. L. Kohlstedt, M. E. Zimmerman, F. Heidelbach, T. Hiraga, and J. Hustoft, (2003), Melt segregation and strain partitioning: Implications for seismic anisotropy and mantle flow, *Science*, *301*, 1227–1230.

Hooper, P. R., V. E. Camp, S. P. Reidel, and M. E. Ross (2007) The origin of the Columbia River flood basalt province: Plume versus nonplume models, in *Plates, Plumes, and Planetary Processes*, edited by G. R. Foulger and D. M. Jurdy, Geol. Soc. Am. Special Pap., *430*, 635–668.

Humphreys, E. D., and D. D. Coblentz (2007), North American dynamics and western U.S. tectonics, *Rev. Geophys.*, *45*, RG3001, doi:10.1029/2005RG000181.

James, D. E., M. J. Fouch, R. W. Carlson, and J. B. Roth (2011), Slab fragmentation, edge flow and the origin of the Yellowstone hotspot track, *Earth Planet. Sci. Lett.*, *311*, 124–135.

Jordan, B. T., A. L. Grunder, R. A. Duncan, and A. L. Deino (2004), Geochronology of age-progressive volcanism of the Oregon High Lava Plains: Implications for the plume interpretation of Yellowstone, *J. Geophys. Res. 109*, B10202, doi:10.1029/2003JB002776.

Jung, H., and S. I. Karato (2001), Water-induced fabric transitions in olivine, *Science*, *293*, 1460–1463.

Jung, H., I. Katayama, Z. Jiang, T. Hiraga, and S. Karato (2006), Effect of water and stress on the lattice preferred orientation (LPO) of olivine, *Tectonophysics*, *421*, 1–22.

Kaminski, É., N. M. Ribe, and J. T. Browaeys (2004), D-Rex, a program for calculation of seismic anisotropy due to crystal lattice preferred orientation in the convective upper mantle, *Geophys. J. Int.*, *158*, 744–752.

Karato, S.-i. (2008), Insights into the nature of plume-asthenosphere interaction from central Pacific geophysical anomalies, *Earth Planet. Sci. Lett.*, *274*, 234–240.

Karato, S.-i., H. Jung, I. Katayama, and P. Skemer (2008), Geodynamic significance of seismic anisotropy of the upper mantle: New insights from laboratory studies, *Annu. Rev. Earth Planet. Sci.*, *36*, 59–95.

Katayama, I., H. Jung, and S. Karato (2004), New type of olivine fabric from deformation experiments at modest water content and low stress, *Geology*, *32*, 1045–1048.

Kelbert, A., G. D. Egbert, and C. deGroot-Hedlin (2012), Crust and upper mantle electrical conductivity beneath the Yellowstone Hotspot Track, *Geology*, *40*, 447–450.

Kendall, J.-M. (1994), Teleseismic arrivals at a mid-ocean ridge: Effects of mantle melt and anisotropy, *Geophys. Res. Lett.*, *21*, 301–304.

Kincaid, C., K. A. Druken, R. W. Griffiths, and D. R. Stegman (2013), Bifurcation of the Yellowstone plume driven by subduction-induced mantle flow, *Nat. Geosci.*, *6*, 395–399.

Kneller, E. A., M. D. Long, and P. E. van Keken (2008), Olivine fabric transitions and shear wave anisotropy in the Ryukyu subduction system, *Earth and Planetary Science Letters*, *268*, 268–282.

Li, A., D. W. Forsyth, and K.M. Fischer (2003), Shear velocity structure and azimuthal anisotropy beneath eastern North America from Rayleigh wave inversion, *J. Geophys Res.*, *108*(B8), 2362, doi:10.1029/2002JB002259.

Lin, F.-C., and M. H. Ritzwoller (2011), Helmholtz surface wave tomography for isotropic and azimuthally anisotropic structure, *Geophys. J. Int.*, *186*, 1104–1120.

Lin, F.-C., M. H. Ritzwoller, Y. Yang, M. P. Moschetti, and M. J. Fouch (2011), Complex and variable crustal and uppermost mantle seismic anisotropy in the western United States, *Nat. Geosci.*, *4*, 55–61.

Liu, K. (2009), NA-SWS-1.1: A uniform database of teleseismic shear wave splitting measurements for North America, *Geochem. Geophys. Geosyst.*, *10*, Q05011, doi:10.1029/2009GC002440.

Liu, L., and D. R. Stegman (2012), Origin of Columbia River flood basalt controlled by propagating rupture of the Farallon slab, *Nature*, *482*, 386–389.

Long, M. D., and T. W. Becker (2010), Mantle dynamics and seismic anisotropy, *Earth Planet. Sci. Lett.*, *297*, 341–354.

Long, M. D., H. Gao, A. Klaus, L. S. Wagner, M. J. Fouch, D. E. James, and E. Humphreys (2009), Shear wave splitting and the pattern of mantle flow beneath eastern Oregon, *Earth Planet. Sci. Lett.*, *288*, 359–369.

Long, M. D., C. B. Till, K. A. Druken, R. W. Carlson, L. S. Wagner, M. J. Fouch, D. E. James, T. L. Grove, N. Schmerr, and C. Kincaid (2012), Mantle dynamics beneath the Pacific Northwest and the generation of voluminous back-arc volcanism, *Geochem. Geophys. Geosyst.*, *13*, Q0AN01, doi:10.1029/2012GC004189.

Mainprice, D. (2007), Seismic anisotropy of the deep Earth from a mineral and rock physics perspective, in *Treatise on Geophysics*, vol. *2*, Mineral Physics, edited by G. Schubert, pp. 437–491. doi:10.1016/B978-044452748-6.00045-6, Elsevier, Oxford, U. K.

Meigs, A., et al. (2009), Geological and geophysical perspectives on the magmatic and tectonic development, High Lava Plains and northwest Basin and Range, in *Volcanoes to Vineyards: Geologic Field Trips Through the Dynamic Landscape of the Pacific Northwest, Geol. Soc. of Am. Field Guide*, vol. *15*, edited by J. E. O'Connor, R. J. Dorsey, and I. P. Madin, pp. 435–470, Geol. Soc. of Am., Boulder, Colo., doi:10.1130/2009.fld015(21).

Monteiller, V., and S. Chevrot (2010), How to make robust splitting measurements for single-station analysis and three-dimensional imaging of seismic anisotropy, *Geophys. J. Int.*, *182*, 311–328.

Nakajima, J., and A. Hasegawa (2004), Shear-wave polarization anisotropy and subduction-induced flow in the mantle wedge of northeastern Japan, *Earth Planet. Sci. Lett.*, *225*, 365–377, doi:10.1016/j.epsl.2004.06.011.

Obrebski, M., R. M. Allen, M. Xue, and S. Hung (2010), Slab-plume interaction beneath the Pacific Northwest, *Geophys. Res. Lett.*, *37*, L14305, doi:10.1029/2010GL043489.

Obrebski, M., R. M. Allen, F. Pollitz, and S.-H. Hung (2011), Lithosphere-asthenosphere interaction beneath the western United States from the joint inversion of body-wave traveltimes and surface-wave phase velocities, *Geophys. J. Int.*, *185*, 1003–1021.

Pierce, K. L., and L. A. Morgan (1992), The track of the Yellowstone hot spot: Volcanism, faulting and uplift, *Mem. Geol. Soc. Am.*, *179*, 1–53.

Precigout, J., and G. Hirth (2011), The origin of olivine B-type fabric in naturally deformed peridotite: Insight from the Ronda large-scale mantle shear zone (Spain), Abstract T43C-2319 presented at AGU Fall Meeting, AGU, San Francisco, Calif.

Richards, M., R. A. Duncan, and V. E. Courtillot (1989), Flood basalts and hot-spot tracks: Plume heads and tails, *Science*, *246*, 103–107.

Roth, J. B., M. J. Fouch, D. E. James, and R. W. Carlson (2008), Three-dimensional seismic velocity structure of the northwestern United States, *Geophys. Res. Lett.*, *35*, L15304, doi:10.1029/2008GL03466.

Schmandt, B., and E. D. Humphreys (2010), Complex subduction and small-scale convection revealed by body-wave tomography of the western United States upper mantle, *Earth Planet. Sci. Lett.*, *297*, 435–445.

Schmandt, B., K. Dueker, E. Humphreys, and S. Hansen (2012), Hot mantle upwelling across the 660 beneath Yellowstone, *Earth Planet. Sci. Lett.,* 331–332, 224–236, doi:10.1016/j.epsl.2012.03.025.

Schutt, D., E. D. Humphreys, and K. Dueker (1998), Anisotropy of the Yellowstone hot spot wake, Eastern Snake River Plain, Idaho, *Pure Appl. Geophys.*, *151*, 443–462.

Shoemaker, K. A. (2004), The tectonomagmatic evolution of the late Cenozoic Owyhee Plateau, northwestern United States, PhD dissertation, Dep. of Geol., Miami Univ., Oxford, Ohio.

Silver, P. G., and M. K. Savage (1994), The interpretation of shear-wave splitting parameters in the presence of two anisotropic layers, *Geophys. J. Int.*, *119*, 949–963.

Silver, P. G. (1996), Seismic anisotropy beneath the continents: Probing the depths of geology, Annual Review of Earth and Planetary Sciences, *24*, 385–432.

Skemer, P., I. Katayama, Z. Jiang, and S.-i. Karato (2005), The misorientation index: Development of a new method for calculating the strength of lattice-preferred orientation, *Tectonophysics*, *411*, 157–167.

Skemer, P., J. M. Warren, P. B. Kelemen, and G. Hirth (2010), Microstructural and rheological evolution of a mantle shear zone, *J. Petrol.*, *51*, 43–53.

Skemer, P., J. M. Warren, and G. Hirth (2012), The influence of deformation history on the interpretation of seismic anisotropy, *Geochem. Geophys. Geosyst.*, *13*, Q03006, doi:10.1029/2011GC003988.

Smith, M. L., and F. A. Dahlen (1973), The azimuthal dependence of Love and Rayleigh wave propagation in a slightly anisotropic medium, *J. Geophys. Res.*, *78*, 3321–3333.

Smith, R. B., M. Jordan, B. Steinberger, C. M. Puskas, J. Farrell, G. P. Waite, S. Husen, W.-L. Chang, and R. O'Connell (2009), Geodynamics of the Yellowstone hotspot and mantle plume: Seismic and GPS imaging, kinematics, and mantle flow, *J. Volcanol. Geotherm. Res.*, *188*, 26–56.

Stachnik, J. C., K. Dueker, D. L. Schutt, and H. Yuan (2008), Imaging Yellowstone plume-lithosphere interactions from inversion of ballistic and diffusive Rayleigh wave dispersion and crustal thickness data, *Geochem. Geophys. Geosyst.*, *9*, Q06004, doi:10.1029/2008GC001992.

Tikoff, B., B. Benford, and S. Giorgis (2008), Lithospheric control on the initiation of the Yellowstone hotspot: Chronic reactivation of lithospheric scars, *Int. Geol. Rev.*, *50*, 305–324.

Till, C. B., T. L. Grove, R. W. Carlson, J. M. Donnelly-Nolan, M. J. Fouch, L. S. Wagner, and W. K. Hart (2013), Depths and temperatures of $<10.5$ Ma mantle melting and the lithosphere-asthenosphere boundary below southern Oregon and northern California, *Geochem. Geophys. Geosyst.*, *14*, 864–879, doi:10.1002/ggge.20070.

Tommasi, A., A. Vauchez, M. Godard, and F. Belley (2006), Deformation and melt transport in a highly depleted peridotites massif from the Canadian Cordillera: Implications to seismic anisotropy above subduction zones, *Earth Planet. Sci. Lett.*, *252*, 245–259.

Vauchez, A., and C. J. Garrido (2001), Seismic properties of an asthenospherized lithospheric mantle: Constraints from lattice preferred orientations in peridotites from the Ronda massif, *Earth Planet. Sci. Lett.*, *192*, 235–249.

Waite, G. P., D. L. Schutt, and R. B. Smith (2005), Models of lithosphere and asthenosphere anisotropic structure of the Yellowstone hot spot from shear wave splitting, *J. Geophys. Res.*, *110*, B11304, doi:10.1029/2004JB00351.

Wagner, L. S., D. W. Forsyth, M. J. Fouch, and D. E. James (2010), Detailed three-dimensional shear wave velocity structure of the northwestern United States from Rayleigh wave tomography, *Earth Planet. Sci. Lett.*, *299*, 273–284.

Wagner, L. S., M. J. Fouch, D. E. James, and S. Hanson-Hedgecock (2012a), Crust and upper mantle structure beneath the Pacific Northwest from joint inversions of ambient noise and earthquake data, *Geochem. Geophys. Geosyst.*, *13*, Q0AN03, doi:10.1029/2012GC04353.

Wagner, L. S., M. J. Fouch, D. E. James, and M. D. Long (2013), The role of hydrous phases in the formation of trench parallel anisotropy: Evidence from Rayleigh waves in Cascadia, *Geophys. Res. Lett.*, *40*, 2642–2646, doi:10.1002/grl.50525.

Wang, Q., Q.-K. Xia, S. Y. O'Reilly, W. L. Griffin, E. E. Beyer, and H. K. Brueckner (2013), Pressure- and stress-induced fabric transition in olivine from peridotites in the Western Gneiss Region (Norway): Implications for mantle seismic anisotropy, *J. Metamorphic Geol.*, *31*, 93–111.

Warren, J. M., G. Hirth, and P. B. Kelemen (2008), Evolution of olivine lattice preferred orientation during simple shear in the mantle, *Earth Planet. Sci. Lett.*, *272*, 501–512.

Warren, L. M., J. A. Snoke, and D. E. James (2008), S-wave velocity structure beneath the High Lava Plains, Oregon, from Rayleigh-wave dispersion inversion, *Earth Planet. Sci. Lett.*, *274*, 121–131.

Weeraratne, D. S., D. W. Forsyth, Y. Yang, and S. C. Webb (2007), Rayleigh wave tomography beneath intraplate volcanic ridges in the South Pacific, *J. Geophys. Res.*, *112*, B06303, doi:10.1029/2006JB004403.

West, J. D., M. J. Fouch, J. B. Roth, and L. T. Elkins-Tanton (2009), Vertical mantle flow associated with a lithospheric drip beneath the Great Basin, *Nat. Geosci.*, *1*, 177–180.

Wüstefeld, A., G. Bokelmann, C. Zaroli, and G. Barruol (2008), SplitLab: A shear-wave splitting environment in Matlab, *Comput. Geosci.*, *34*, 515–528.

Xue, M., and R. M. Allen (2006), Origin of the Newberry Hotspot Track: Evidence from shear-wave splitting, *Earth Planet. Sci. Lett.*, *244*, 315–322.

Yang, Y., and D. W. Forsyth (2006), Regional tomographic inversion of the amplitude and phase of Rayleigh waves with 2-D sensitivity kernels, *Geophys. J. Int.*, *166*, 1148–1160.

Yuan, H., and B. Romanowicz (2010), Depth dependent azimuthal anisotropy in the western US upper mantle, *Earth Planet. Sci. Lett.*, *300*, 385–394.

Zandt, G., and E. Humphreys (2008), Toroidal mantle flow through the western U.S. slab window, *Geology*, *36*, 295–298.

Zandt, G., H. Gilbert, T. J. Owens, M. Ducea, J. Saleeby, and C. H. Jones (2004), Active foundering of a continental arc root beneath the southern Sierra Nevada in California, *Nature*, *431*, 41–46.

Zhou, Y., F. A. Dahlen, and G. Nolet (2004), Three-dimensional sensitivity kernels for surface wave observables, *Geophys. J. Int.*, *158*, 142–168.